10 Advanced Optical Metrology

Particles I

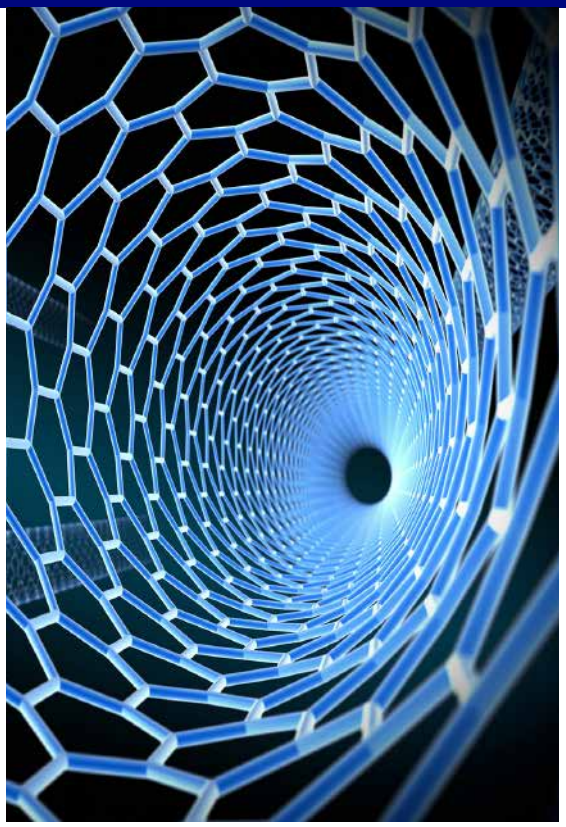

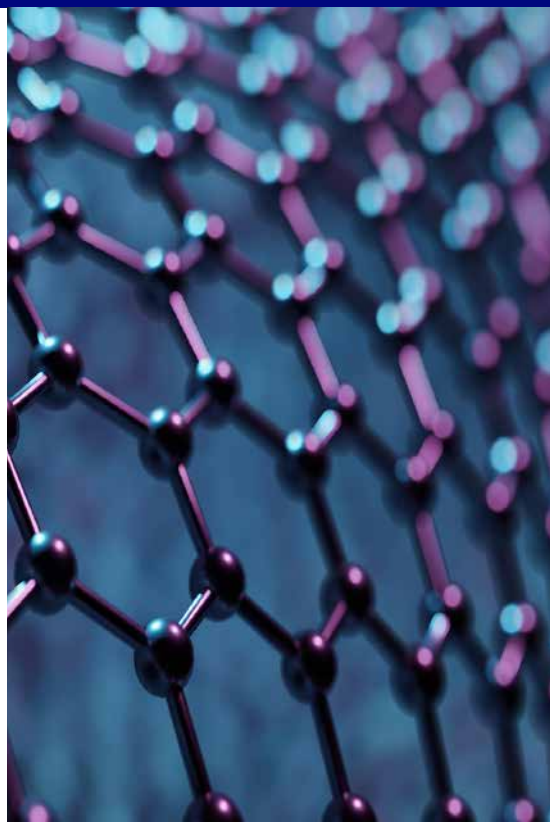

OLYMPUS

WILEY

Contents

Imprint

© Wiley-VCH GmbH
Boschstr. 12,
69469 Weinheim, Germany
Email: info@wiley-vch.de
Editor-in-Chief: Dr. Christina Poggel

Introduction

The term particle is derived from Latin, where the prefix "part" means a portion of something, and the suffix "–icle" is equivalent to small. Its meaning depends on the subject but is generally used to name a portion of matter with reduced dimensions. There is a whole field called particle physics that studies the elemental particles that form matter. However, elemental particles like electrons, protons, quarks, etc., are not what chemists and materials scientists mean when they refer to particles. For them, a particle is the smallest fragment of matter that maintains the chemical properties of a body. In this sense, atoms and molecules are particles, but most of the time, the term particle is used to refer to micro and nanoparticles.

A nanoparticle is a particle with a size between 1 and 100 nm, although the term is used for particles up to 500 nm and for fibers, tubes, or rods that are less than 100 nm in at least one dimension.[1] Metal particles smaller than 1 nm are referred to as "atom clusters." Other classes include microparticles (1–1000 µm), fine particles (100–2500 nm), and coarse particles (2500–10000 nm).

UNIQUE PROPERTIES

Nano and microparticles are distinctive materials that have enormous technological and scientific value. They are used in many applications, including energy, medical, and environmental. Even though nano and microparticles have the same composition as analogous bulk material, they display very interesting optical, electrical, thermal, and magnetic properties. Materials science has developed several methods to tune these properties for specific applications.

Nano and microscale particles have two technologically relevant features. First, particulate systems have a very high surface-to-weight ratio. As a result, surface energies are large with respect to volumes, and, therefore, the energetics of reactions (and rates) are different. This characteristic makes them valuable for a wide range of applications such as coatings, catalysts, adsorbents, and more. On the other hand, when the scale is about a few nanometers, new properties and new striking phenomena take place.

Properties such as melting point, fluorescence, electrical conductivity, magnetic permeability, and chemical reactivity change as a function of the particle's size.[2] For example, at the nanoscale, quantum effects are dominant, which is why semiconductor quantum dots emit different wavelengths of light depending on their nano-size.[3] Another example is magnesium (Mg), where the number of atoms and the size of the cluster/particle, determines the electronic band gap of the material. The electronic proper-

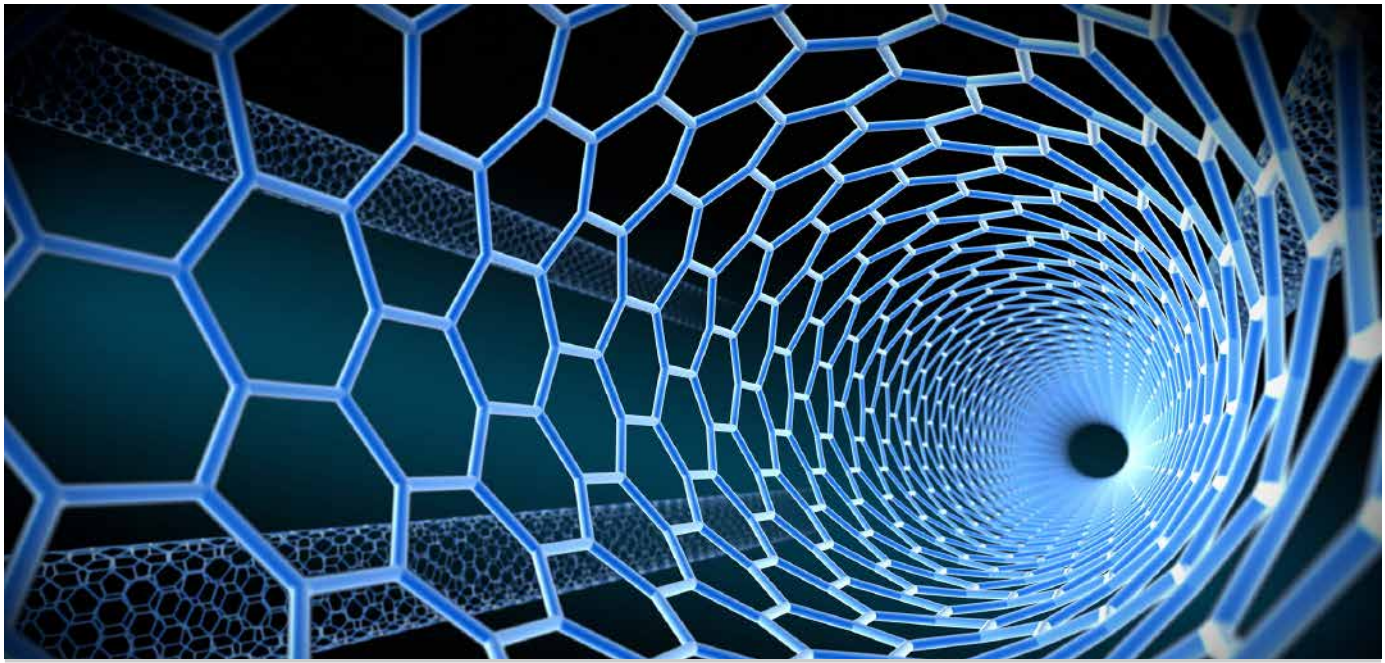

Figure 1

ties of the clusters or particles change from a semi-conductor (<18 atoms) to metallic.[4]

Nanoparticles made of gold and silver exhibit size-dependence in their optical properties. [6] For example, Figure 2 shows where different shapes and sizes determine a material's optical properties. Gold and silver nanoparticles absorb and scatter light very efficiently. They interact strongly with light because the conductive electrons on the metal surface undergo a collective oscillation when they are excited by light at specific wavelengths; this is known as surface plasmon resonance (SPR). The absorption and scattering properties of these nanoparticles can be tuned by controlling the particle size, shape, and the local refractive index near the particle surface.[6]

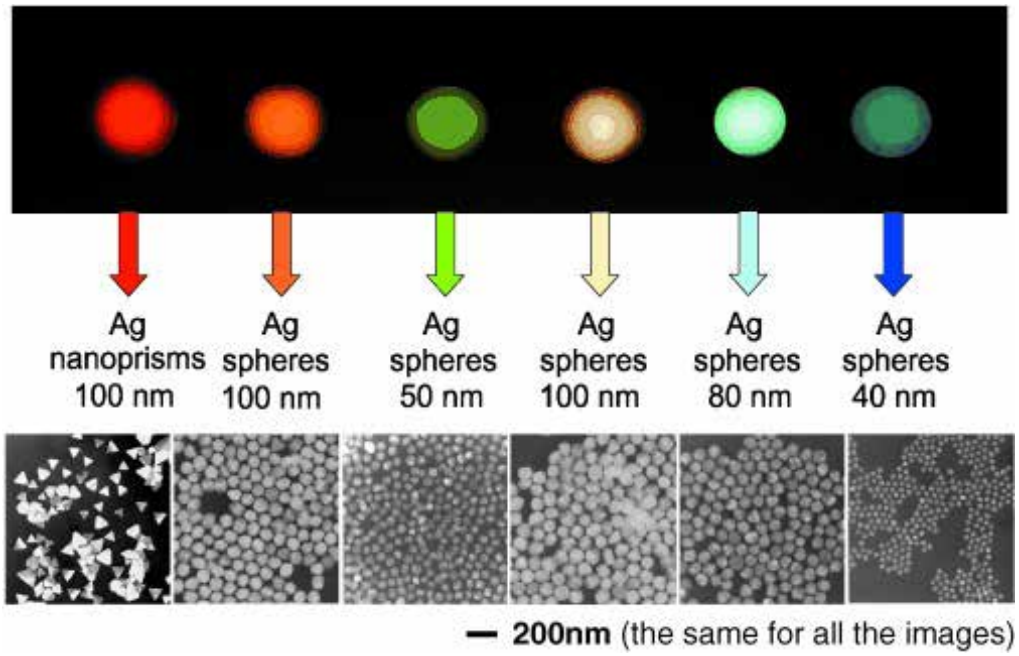

Figure 2: Size, shape, and composition determines the Rayleigh light-scattering properties of various nanoparticles.[8]

Gold and silver nanoparticles have diverse applications in drug delivery, such as determining and sensing drugs in pharmaceuticals.[7]

DIVERSE SHAPES AND SYNTHESIS PATHS

Based on their shape, nanoparticles can occur as nanosheets or nanofilms, which have at least one dimension in this size range; and nanorods and nanoparticles, which have two and three dimensions in this size range, respectively. There are also nanotubes, which are nanoscale materials that have a tube-like structure (e.g., carbon nanotubes).

Nano and microparticles are usually synthesized using physical and chemical methods. In physical methods, particles are generated by decreasing the size of the source material (top-down approach). Physical techniques include milling, gas condensation, electro-spraying, lithography, and thermal decomposition. On the other hand, in chemical methods, particles are created by nucleating and growing particles from atomic or molecular precursors in the liquid or vapor phase of a chemical reaction (bottom-up approach). Chemical methods include microemulsion, emulsion polymerization, hydrothermal, microfluidic, chemical vapor, pyrolysis, and sol-gel processes. Chemical methods generate nanostructures with fewer defects, enable more complex and homogeneous compositions, and are easily scalable for low-cost and rapid fabrication.

UNCOUNTABLE APPLICATIONS

Several industries benefit from nano and microparticles. The microelectronics industry—one of the first to use nanoparticles—supplies an annual market of 500,000 million dollars (2016).[9] Today, medicine is one of the most promising areas for the application of microparticles to treat specific diseases, as drug delivery systems and/or nano/micro-actuators.[10] Moreover, in the field of energy, microparticles are being used to develop systems with greater energy storage capacity, as in the case of carbon nano tubes in modern batteries.[9] Likewise, energy capture capacity can lead to the development of devices that produce their own energy with a significant advantage over wiring or batteries. The food industry also sees advantages in the use of nanoparticles, since they can be used to detect changes in food at early stages, helping avoid contamination prior to consumption.[9]

As our understanding of how we can develop and improve the synthesis and characterization methods of nano and microparticles, we will continue to find new applications that help solve global challenges in applications like energy, health, and food, positively impacting our daily lives thanks to their fascinating and tunable properties.

REFERENCES

[1] *A.C. Grimsdale, K. Müllen, The Chemistry of Organic Nanomaterials, Angew. Chemie Int. Ed. 44 (2005) 5592–5629. https://doi.org/10.1002/anie.200500805.*

[2] *K. Yoshihara, M. Sakamoto, H. Tamamitsu, M. Arakawa, K. Saitow, Extraordinary Field Enhancement of TiO 2 Porous Layer up to 500-Fold, Adv. Opt. Mater. 6 (2018) 1800462. https://doi.org/10.1002/adom.201800462.*

[3] *D. Ren, B. Wang, C. Hu, Z. You, Quantum dot probes for cellular analysis, Anal. Methods. 9 (2017) 2621–2632. https://doi.org/10.1039/C7AY00018A.*

[4] *O.C. Thomas, W. Zheng, S. Xu, K.H. Bowen, Onset of Metallic Behavior in Magnesium Clusters, Phys. Rev. Lett. 89 (2002) 213403. https://doi.org/10.1103/PhysRevLett.89.213403.*

[5] *Introduction to Nanoscience: Some Basics, (n.d.). https://serc.carleton.edu/msu_nanotech/nano_intro.html.*

[6] *A.J. Haes, C.L. Haynes, A.D. McFarland, G.C. Schatz, R.P. Van Duyne, S. Zou, Plasmonic Materials for Surface-Enhanced Sensing and Spectroscopy, MRS Bull. 30 (2005) 368–375. https://doi.org/10.1557/mrs2005.100.*

[7] *K. Alaqad, T.A. Saleh, Gold and Silver Nanoparticles: Synthesis Methods, Characterization Routes and Applications towards Drugs, J. Environ. Anal. Toxicol. 6 (2016). https://doi.org/10.4172/2161-0525.1000384.*

[8] *C.A. Mirkin, The Beginning of a Small Revolution, Small. 1 (2004) 14–16. https://doi.org/10.1002/smll.200400092.*

[9] *C.R. Kagan, L.E. Fernandez, Y. Gogotsi, P.T. Hammond, M.C. Hersam, A.E. Nel, R.M. Penner, C.G. Willson, P.S. Weiss, Nano Day: Celebrating the Next Decade of Nanoscience and Nanotechnology, ACS Nano. 10 (2016) 9093–9103. https://doi.org/10.1021/acsnano.6b06655.*

[10] *D. Ditter, P. Blümler, B. Klöckner, J. Hilgert, R. Zentel, Microfluidic Synthesis of Liquid Crystalline Elastomer Particle Transport Systems which Can Be Remote-Controlled Magnetically, Adv. Funct. Mater. 29 (2019) 1902454. https://doi.org/10.1002/adfm.201902454.*

01 Microfluidic Synthesis of Liquid Crystalline Elastomer Particle Transport Systems that Can Be Remote-Controlled Magnetically

D. Ditter, P. Blümler, B. Klöckner, *et al.*

ABSTRACT

The synthesis of liquid crystalline elastomer (LCE) particles, which can be remote-controlled magnetically and used as transport systems, is presented for the first time. Ferri-magnetic, rod-shaped Fe_3O_4 nanoparticles are functionalized to make them compatible with organic LCE precursor compounds. Their influence on the LCE precursor alignment is studied and thermoresponsive as well as photoresponsive LCE microparticles are synthesized with a microfluidic device. The potential of synthesized LCE particles as transport systems is demonstrated by the transport of plastic, textiles, or copper, which can be pushed just due to magnetic forces or transported in general by taking advantage of the phase-dependent "stickiness" of LCEs. These studies open doors to novel applications of LCEs as microrobots using magnetism as a control.

INTRODUCTION

The interest for microactuators grow constantly.[1–4] Recently, a transition from hard and rigid to soft and flexible microactuators took place, probably because of the easy corrosion and low biocompatibility of hard actuators.[5,6] An emerging smart soft actuator material is liquid crystalline elastomers (LCEs), which can be triggered with diverse stimuli fields like heat, light, or electric.[7,8] They consist of mesogenic groups, which are incorporated in an elastomer network and thus combine the orientational order of the LC phase with rubber elasticity.[9,10]

To move LCEs magnetically, they have to be made magnetic. An approach to realize this is the integration of magnetic components like ferri-magnetic Fe_3O_4 nanoparticles. For this purpose, such inorganic nanoparticles can be functionalized with polymers to make them compatible with the organic LC matrix.[11] So far, LCEs containing magnetic nanoparticles were mainly synthesized to trig-

ger their phase transition/actuation through heating with AC electromagnetic fields.[8,11,12] However, to the best of our knowledge, no attempts were made to use magnetism for a controlled movement of LCE particles in space.

In this publication we present a route to synthesize a large amount of thermo- and photoresponsive LCE microparticles with a microfluidic setup. They can be moved in magnetic fields with high precision and are suitable as transport systems.

MATERIALS AND METHODS

Materials and Reagents

The liquid crystalline monomers, crosslinker, the dye for the initiator, the Fe_3O_4 nanorods were synthesized as described in the literature (see doi.org/ 10.1002/adfm.201902454 for references). 1,6-Hexanediol diacrylate was purchased from Alfa Aesar. The photoalignment material ROP-108 EXP001 was purchased from Rolic Technologies Ltd. 4-Cyano-4-(thiobenzoylthio)pentanoic acid and the silicone oils (100 cSt and 1000 cSt) were purchased from Sigma Aldrich. Hydrofluoroether Novec HFE-7300 was purchased from 3M. Microscope slides (size: 76 × 26 mm, thickness: 1 mm) were purchased from CARL ROTH. Tetrahydrofuran was purchased from Fisher Scientific. Ethanol and Hellmanex III concentrate were purchased from VWR Chemicals. Butyryl choline butyltriphenylborate (Borat V) was purchased from Spectra group limited.

PTFE tubings for the microfluidic device were purchased from WICOM. Fused silica capillary, T-junction, nuts and ferrules for the microfluidic device were purchased from Postnova Analytics GmbH. The coldlight source KL 1600 was purchased from Schott. The red light HighPower LED (623 nm) was purchased from Conrad.

Characterization of Polymers

^{1}H-NMRs and ^{19}F-NMRs were measured using a 300 MHz spectrometer (model: Avance III HD 300) from Bruker. GPC was measured in THF with polystyrene as an external and toluene as an internal standard. A refractive index detector (G 1362 RID) and a UV/vis detector (UV-2075 Plus) from Jasco were used to detect the polymers. IR spectroscopy was performed using a FT/IR-4100 from Jasco. Spectra were analyzed with a Spectra Manager 2.0 from Jasco. UV/vis spectra were measured with a Jasco spectrophotometer V-630. Spectra were analyzed using Spectra Manager 2 from Jasco. TGA measurements were performed with a Perkin Elmer Pyris 6 under nitrogen flow using a heating rate of 10 °C (50 °F) min−1 (50–700 °C or 122–1292 °F). TEM measurements were performed on a Tecnai G2 Spirit (FEI) at 120 kV using a 2_2k camera.

LC Phase Analysis of Fe_3O_4 Containing LCE Precursors

Microscope slides were cut into 25 × 25 mm pieces, rinsed with a Hellmanex III solution, deionized water, and ethanol for 3 min respectively, dried with a nitrogen stream, and treated with oxygen plasma in a plasma oven (model: PlasmaPrep5) from Gala Instrumente GmbH for 5 min with a power of 100 W.

40 µL photoalignment layer solution ROP-108 EXP001 was spin-coated dynamically at 2000 rounds per minute (rpm) for 60 s on top of the microscope slides, dried at 150 °C (302 °F) for 10 min on a hot plate, allowed to cool down to room temperature, and irradiated with linear polarized UV-light (UV source: Oriel LSH302 (500 W lamp)) with an angle of incidence of 90° through a polarizer from Olympus® U-POT Japan (>300 nm) for 10 min. 10 mg of the particular LCE precursor (formulation 1a without or including 45 mol% comonomer 3 and formulation 1b) containing 0, 5, and 10 wt% (wt% referred to the monomer(s)/crosslinker mixture) Fe_3O_4 was dissolved in 100 µL THF and spin-coated dynamically with 3000 rpm on top of the alignment layer.

LCE precursor films were heated in their LC phase with a hot stage (model: Linkam TMS 94) and investigated via polarized optical microscopy (model: Olympus BX51 microscope). Images were taken with a microscope camera (model: Olympus DP22 camera) and analyzed using the imaging software Cell^D.

Analysis of LCE Actuations

Thermal and photochemical actuations of all LCE particles were investigated using a light microscope (model: Olympus BX51 microscope) equipped with a microscope camera (model: Olympus DP22 camera) and a hot stage (model: Linkam TMS 94) to set the desired temperature. The LCE particles were heated from the LC to the isotropic phase (80 to 130 °C or 176 ° to 266 °F) for thermoresponsive LCEs synthesized out of formulation 1a without comonomer 3; 50 to 100 °C (122 to 212 °F) for thermoresponsive LCEs synthesized out of formulation 1a including 45 mol% comonomer 3; 40 to 110 °C (104 to 230 °F) for photoresponsive LCEs synthesized out of formulation 1b)

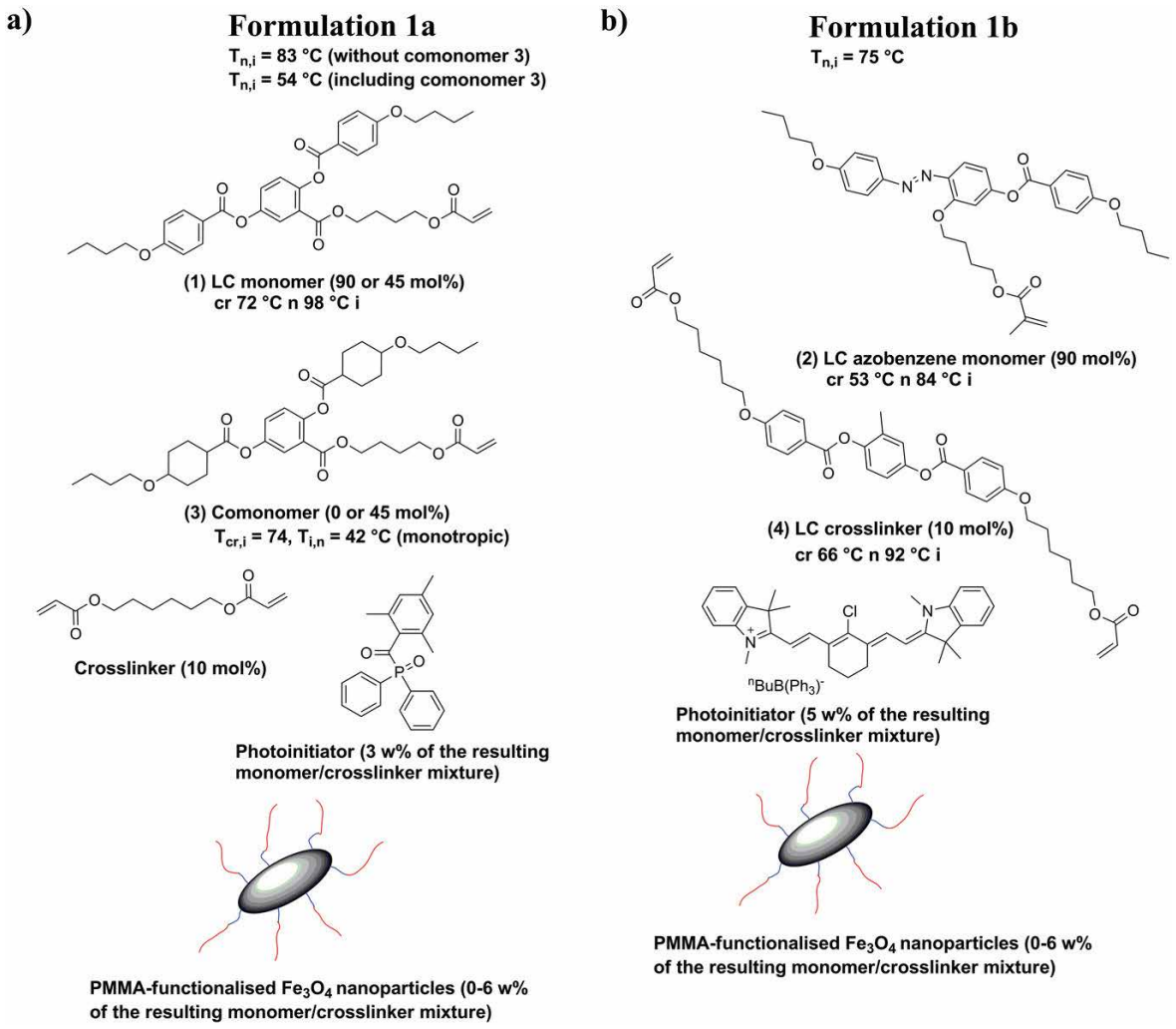

Figure 1: a) Thermoresponsive LCE precursor consisting of LC monomer 1 (4′-acryloyloxybutyl 2,5-(4′-butyloxybenzoyloxy)benzoate) (90 mol%) or a mixture of LC monomer 1 (45 mol%) and comonomer 3 (4′-acryloyloxybutyl 2,5-di(4′-pentylcyclohexyloyloxy)benzoate) (45 mol%), a crosslinker (1,6-hexandioldiacrylate) (10 mol%), a UV-initiator (diphenylphosphine oxide or TPO) (3 wt% referred to the monomer/crosslinker mixture), and PMMA functionalized Fe_3O_4 nanorods (0–6 wt% referred to the monomer/crosslinker mixture). b) Photoresponsive LCE precursor consisting of LC azobenzene monomer 2 (4-butoxy-2′-(4-methacryloyloxybutoxy)-4′-(4-butoxybenzoyloxy)azobenzene) (90 mol%), LC crosslinker 4 (2-methyl-1,4-phenylene bis(4-((6-(acryloyloxy)hexyl)oxy)benzoate)) (10 mol%), a NIR initiator (1,3,3,1′,3′,3′-hexamethyl-11-chloro-10,12-propylene-tricarbocyanine triphenylbutyl borate or CBC) (5 wt% referred to the monomer/crosslinker mixture), and PMMA functionalized Fe_3O_4 nanorods (0–6 wt% referred to the monomer/crosslinker mixture).

and their sizes were analyzed using the imaging software Cell^D. Irradiation of the photoresponsive samples were performed at 70 °C (158 °F) with the coldlight source KL 1600 using light guides to focus the light on samples. Irradiation with red light was performed with the help of a red-light filter from Schott (>500 nm), which was held in the light beam.

See the original article and supporting information for all experimental procedures (doi.org/ 10.1002/adfm.201902454).

RESULTS AND DISCUSSION

Synthesis of PMMA Functionalized Anisotropic Fe_3O_4 Nanoparticles

Rod-shaped, ferri-magnetic Fe_3O_4 nanoparticles were made compatible with organic LCE precursors through functionalization with poly(methyl methacrylate) (PMMA). Hereby, stable suspensions could be obtained, especially when the LC precursor monomers are heated into their isotropic phase. The reaction scheme to obtain PMMA functional-

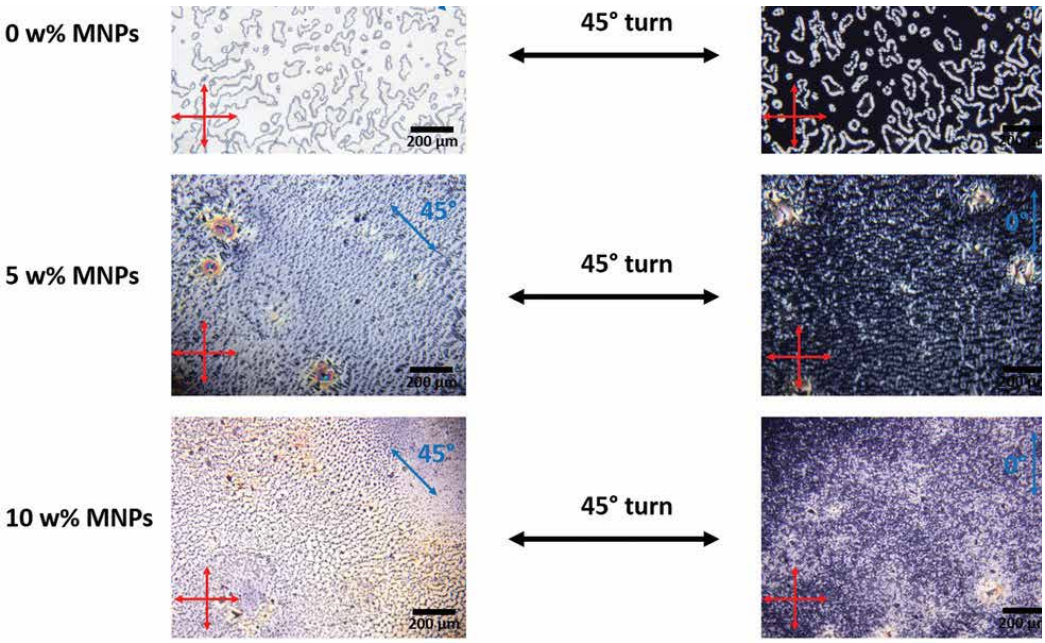

Figure 2: POM images of thermoresponsive LCE precursor mixtures 1a which are spin coated on top of a photoalignment layer and heated into the LC phase (70 °C or 158 °F). It is shown that the contrast of dark and bright states–when the director lies parallel or at a 45° angle regarding to the crossed polarizers–decrease with increasing amounts of MNPs. Thus, it can be concluded that MNPs disturb the alignment. The red arrows indicate the position of the crossed polarizers, and the blue arrows indicate the director's alignment (scale bar: 200 µm).

ized magnetic nanoparticles (MNPs) follows a previously described procedure[13].

Anisotropic, magnetic Fe_3O_4 nanoparticles were synthesized through reduction of Fe_3O_4 particles under a hydrogen/ nitrogen atmosphere. Functionalized Fe_3O_4 nanorods had a length of about 340 nm and a length to width ratio of 4.4 to 1, which was proofed via transmission electron microscopy.

Functionalization of magnetic nanoparticles (MNPs) was done via a grafting-to process with poly(methyl methacrylate-b-dopamine acryl amide) (P(MMA-b-DOPA)). The ratio between the PMMA block and the DOPA block was determined to be 10:1 (by 1H-NMR spectroscopy).

Integration of MNPs into LCE Precursors and their Influence on LC Alignment

The functionalized nanoparticles should be integrable homogeneously into organic thermoresponsive and photoresponsive LCE precursor mixtures. To demonstrate this, two LCE precursor systems were chosen. Their ingredients, including functionalized nanoparticles, are shown in **Figure 1a, b.**

To show the solubility of MNPs in LCE precursors, the ingredients of formulation 1a and 1b were dissolved in tetrahydrofuran, mixed, and the solvent was evaporated afterward. The amount of MNPs was varied between 0 and 10 wt%. While formulations without MNPs were colorless (formulation 1a) or showed an orange color (formulation 1b), the brown color of functionalized Fe_3O_4 particles was adopted with increasing MNP amount. This homogeneous color change of the LCE precursors without observing any aggregates by bare eye is a first proof of compatibility.

To take a closer look, we spin-coated thin films of formulations 1a and 1b containing different amounts of MNPs on a photoalignment layer. Afterward we annealed the films in their LC phase. Thereafter, the dispersions were investigated with polarized optical microscopy (POM). POM images of films of the thermoresponsive system 1a (without comonomer 3) including 0, 5, and 10 wt% MNPs are presented in **Figure 2.**

All films (this was also found for the other mixtures) showed dark and bright states when the director was oriented parallel or at a 45° angle regarding to the crossed polarizers. The contrast between dark and bright states indicates the quality of alignment. It can be observed that with increasing amount of MNPs the contrast and thus the director alignment decreases or is partially not present anymore. The reason for this is probably that the surface of the MNPs disturbs the director field of the LC phase. This observation already allows predicting that the magnitude of actuation of the LCEs should decrease with increasing

Fe_3O_4 nanoparticle amount since the MNPs reduce the homogeneity of the director field.

Microfluidic Synthesis and Actuation Properties of Magnetic Thermoresponsive and Photoresponsive LCE Particles

To synthesize LCE particles with a microfluidic setup, precursors were dissolved in THF, stirred to ensure homogeneous dispersions, and the THF was evaporated under reduced pressure. Precursors were then inserted in the microfluidic device. The mixtures were pumped through the device by a low viscous silicon oil at 90 °C (194 °F) (isotropic phase of the LC monomers) to melt them and to obtain the nanoparticles homogeneously dispersed in the isotropic phase. Precursor droplets were formed at the end of a glass capillary. The droplets were then guided over a precision hot plate and polymerized and crosslinked in their LC phase. Alignment was obtained through shear forces. In this way photoresponsive as well as thermoresponsive LCEs containing 0–6 wt% MNPs regarding to the respective monomer/crosslinker mixture were prepared. Thermoresponsive LCEs containing 45 mol% comonomer 3 were synthesized with MNP amounts of 3 and 6 wt%.

Thermal and photochemical actuations were analyzed with an optical microscope by heating them from their LC to their isotropic state. Examples of actuations of a thermoresponsive and a photoresponsive micron-sized LCE particle, including 3 wt% MNPs, are shown in **Figure 3.** The actuations are reversible at least up to 10 actuation cycles. This proves that well crosslinked LCEs are obtained under these conditions.

In **Figure 3,** the thermal and photochemical LCE actuation properties in dependence of their amount of MNPs of the different systems are presented. In general, actuation decreases with increasing amounts of nanoparticles, thus confirming that MNPs disturb the director orientation (see Section 2.2). Particles without MNPs showed thermal actuations of about 40%, which is typical for this kind of LCEs.[14–16] When increasing the Fe_3O_4 amount from 0 to 6 wt%, thermal actuations decrease from about 40% to 30% (ther-

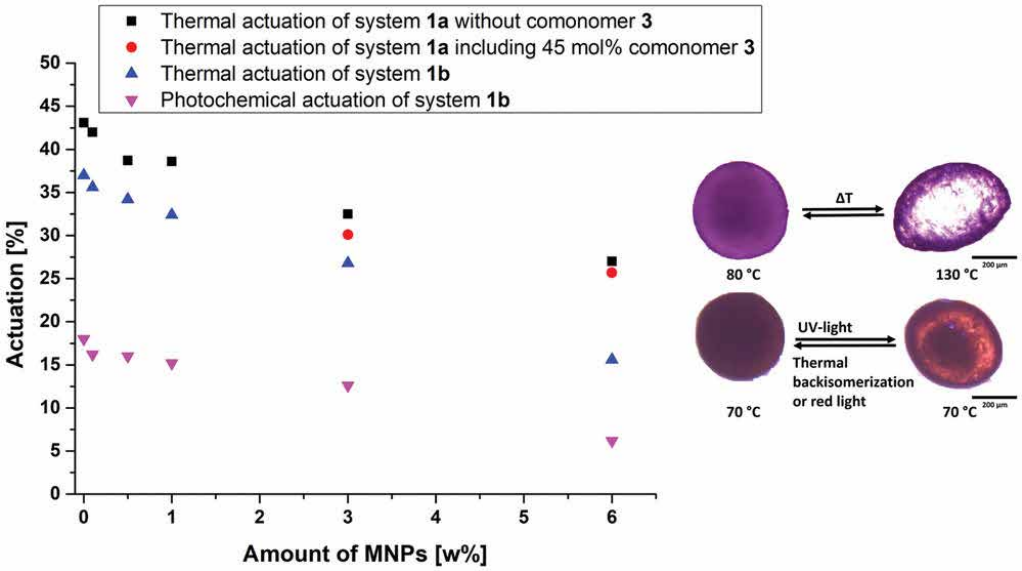

Figure 3: Thermal actuations of the thermoresponsive LCE systems synthesized out of precursor 1a without and including 45 mol% comonomer 3 as well as thermal and photochemical actuations of the photoresponsive LCE system synthesized out of precursor 1b in dependence of their amount of MNPs. On the right side, examples of thermal and photochemical actuations of magnetic LCE microparticles are shown. Upper actuation: Thermal actuation between 80 and 130 °C (176 and 266 °F) of a LCE particle (synthesized out of formulation 1a without comonomer 3) containing 3 wt% Fe_3O_4 particles. Lower actuation: Photochemical actuation of a LCE particle (synthesized out of formulation 1b) containing 3 wt% Fe_3O_4 particles (scale bar: 200 µm).

moresponsive system 1a without comonomer 3) or 15% (photoresponsive system 1b). Photochemical actuations of LCEs synthesized out of formulation 1b decrease from 18% to 6%. Comonomer containing LCEs showed thermal actuations of about 30%, which is slightly below the values of LCEs without comonomer 3, while the actuation temperature decreased from 90–130 to 50–90 °C (194–266 to 122–194 °F). We defined thereby the actuation as the difference of particle length before and after actuation divided by the shorter length (always the dimension in which the particle length increases during heating or UV-irradiation has been regarded).

Guiding of LCE Particles with Magnetic Forces

For the experiments, particles were placed on the surfaces of different fluids that were filled in a glass vial, and a bar magnet was brought in their proximity. Thermo- as well as photoresponsive particles containing 0.5 to 6.0 wt% MNPs followed the magnetic field of the bar magnet on the surfaces whereby the speed increased with increasing amount of MNPs. This trend is not surprising since a higher amount of MNPs increases their magnetism. However, LCE particles containing less than 0.5 wt% MNPs did not follow the bar magnet because they are not or insufficiently magnetizable.

A magnetic setup[17] was used to move particles in the centimeter range with a precision in the submillimeter range. The permanent magnetic device consists of a coaxial arrangement of two Halbach cylinders. The setup was placed under a microscope, and particles inside a glass vial were placed in the middle of the setup on top of a copper block that was heated with a hot plate below to guide particles at different temperatures. To demonstrate magnetic guiding with this device, magnetic LCE particles were moved along a rectangular path. This is presented in **Figure 4a.** We show two particles at once to demonstrate that a collective movement is possible too. Here, it has to be mentioned that those particles tend to stick together in the magnetic setup due to their magnetic dipoles. Additionally, particles can be rotated around themselves through a magnetic stirrer that is shown in **Figure 4b.** To demonstrate that, in general, all kinds of desired movements are possible, we used the two particles shown in **Figure 4a** to "write" LCE on a DMSO layer. It has to be considered that the magnetic force of

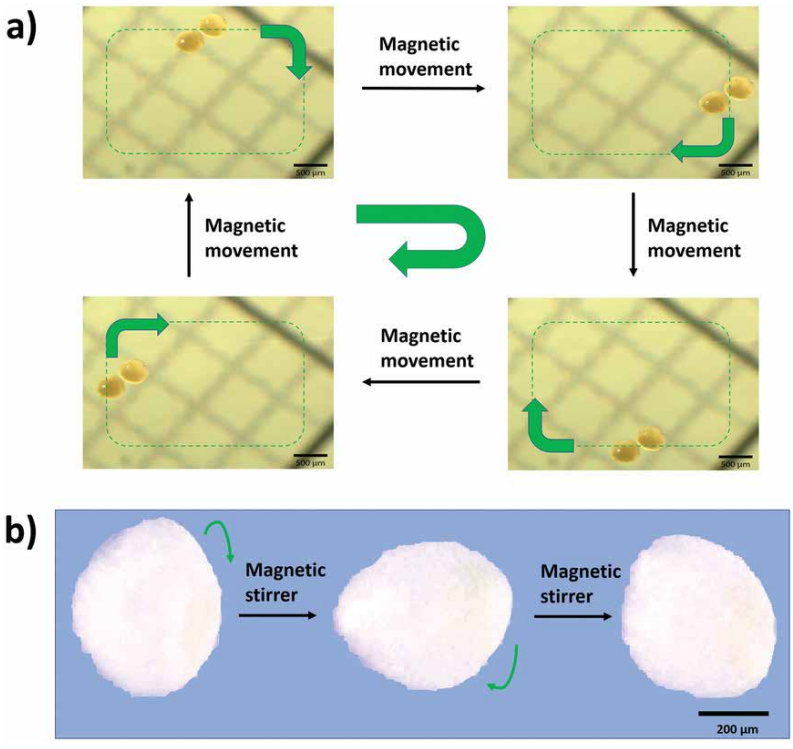

Figure 4: Movements of magnetic LCE particles with magnetic forces. a) Rectangular-like movement of two thermoresponsive magnetic LCE particles (synthesized out of formulation 1a without comonomer 3) containing 6 wt% ferri-magnetic Fe_3O_4 particles caused by the magnetic fields generated by the device shown in **Figure 4e.** The direction of movement is changed by varying the angle between the dipole and quadrupole. The desired moving path is indicated by a dashed green rectangle. The moving direction is indicated by green arrows (scale bar: 500 µm). b) Rotation of a thermoresponsive magnetic LCE particle (synthesized out of formulation 1a without comonomer 3) containing 3 wt% ferri-magnetic Fe_3O_4 particles. The rotation is caused by a magnetic stirrer (scale bar: 200 µm).

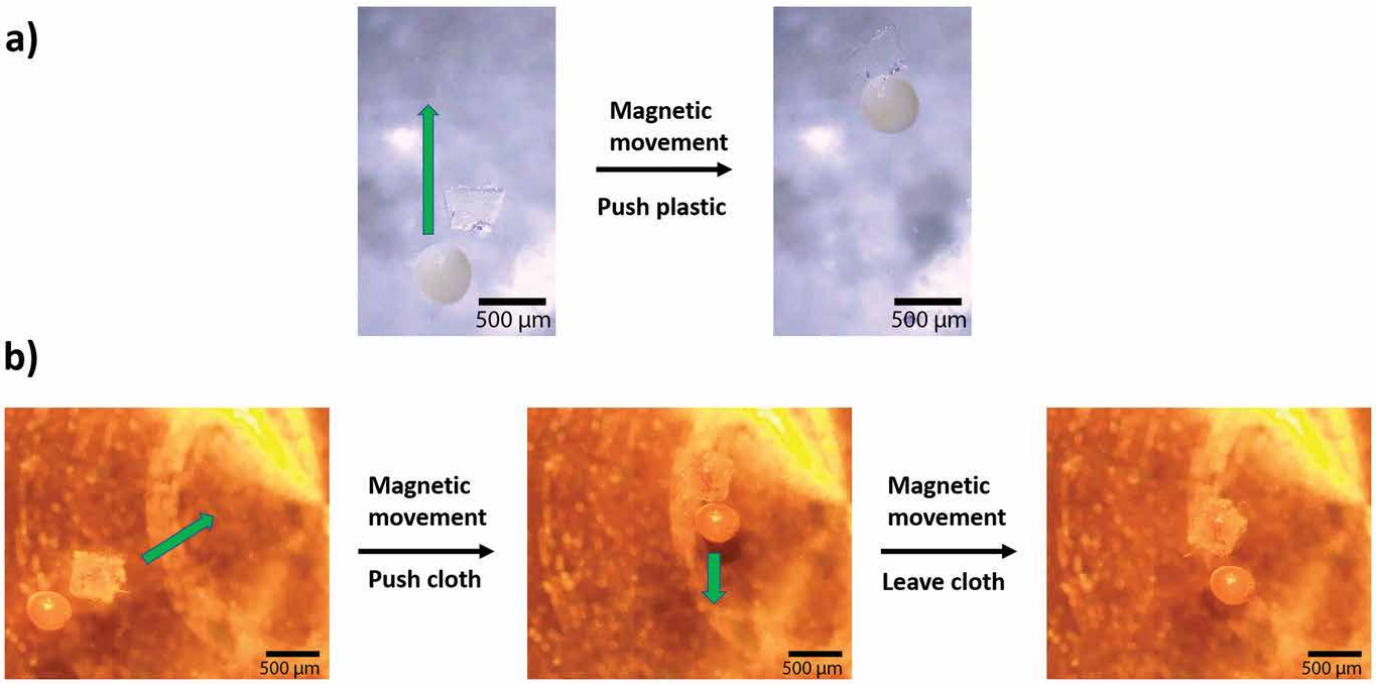

Figure 5: Pushing of a piece of a) plastic with a thermoresponsive LCE particle (synthesized out of formulation 1a without comonomer 3) containing 6 wt% ferri-magnetic Fe_3O_4 or b) textile with a photoresponsive magnetic LCE particle (synthesized out of formulation 1b) containing 6 wt% ferromagnetic Fe_3O_4 on top of a DMSO surface. Pushing is caused exclusively through magnetic forces caused by the magnetic setup shown in **Figure 4e.** The direction of movement is indicated by green arrows. The direction of movement is changed by varying the angle between the dipole and quadrupole (scale bar: 500 µm).

this setup is weaker in comparison to the bar magnet. Thus, magnetic particles including at least 3 wt% MNPs were necessary to observe a movement in the middle of the device.

Combination of Guiding and Actuation of LCE Particles in Magnetic Fields

To demonstrate the combination of guidance and actuation, we moved a photoresponsive LCE particle (synthesized out of formulation 1b) in a circle-like form on a DMSO surface at 70 °C (158 °F) and irradiated it with UV-light, which caused an actuation of 12.6% at a desired position. Generally, the thermoresponsive systems could be actuated by temperature variations. Since heating of the liquids takes, however, much time and as the particles can rotate (tumble around) on the surface it is not so easy to perform a well-controlled actuation just by heating. Nevertheless, reversible actuations were observed proving that the used fluids do not affect LCEs—for example—through swelling.

Magnetic LCE Particles as Transport Systems

The potential of the magnetic LCE particles as transport systems was investigated. For this, nonmagnetic materials like textiles, copper, or plastic were used as transport goods. There are two possibilities for transportation. First, the pure magnetic forces can be used to guide the LCE particles to other microparticles and push them ahead of themselves in the desired directions. This is shown in **Figure 5** where pieces of plastic and textiles are transported. However, with this approach it is just possible to push something and thus, if the direction of transportation needs to be changed, it is necessary that LCE particles leave the materials first and have to be brought to them from another direction again. To avoid this and to open the possibility to pull something, it is, however, possible to use the different stickiness of LCEs in their LC and isotropic phase.

During our experiments we recognized that nonmagnetic particles tend to stick to LCEs in their LC phase and leave the LCEs when they are brought in their isotropic phase. The reason for this is probably that LCEs become softer in the isotropic phase and thus it is easier for other micro-objects to leave the particles when they were tacked before.

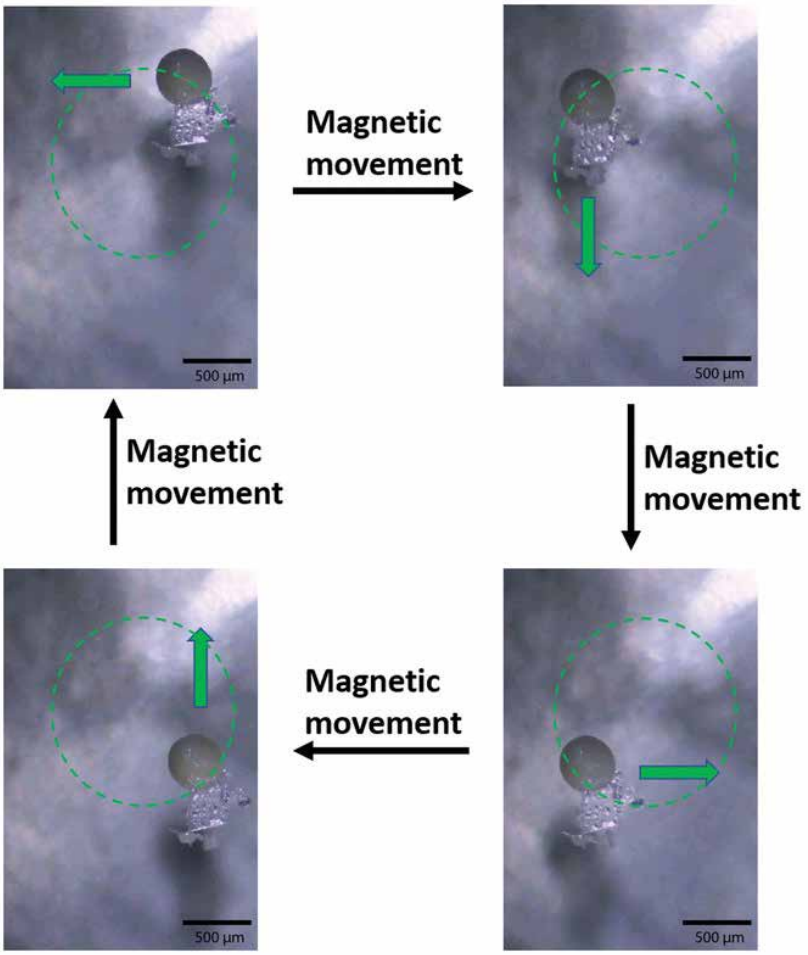

Figure 6: Circle-like transportation of a piece of plastic of a thermoresponsive magnetic LCE particle (synthesized out of formulation 1a without comonomer 3) containing 6 wt% ferri-magnetic Fe_3O_4 on top of a DMSO surface caused by the magnetic setup shown in **Figure 4e.** The desired movement path is indicated by the dashed green circle. The moving direction is indicated by green arrows. The direction of transportation is changed by varying the angle between the dipole and quadrupole (scale bar: 500 µm).

The trend of other objects to stick to the LCE particles was strongest if they got in contact with them in the isotropic phase and cooled down into the LC phase afterward. The reason for this might be that the objects are pushed easily into the soft isotropic LCE particles so that a large connecting interface is created. After cooling the LCE particles down, the objects cannot escape as the particles are in their tougher LC phase. As a result, they work like grippers. Hereby, objects can be transported (pushed and pulled) with the used magnetic setup what is demonstrated as a circle-like transportation of plastic in **Figure 6.**

CONCLUSION

Photoresponsive and thermoresponsive LCE microparticles, which can be moved magnetically and serve as actuators and transport systems, could be synthesized with a microfluidic device for the first time. Fe_3O_4 MNPs were integrated in these particles through functionalization with PMMA. The particles could be remote controlled magnetically on fluidic surfaces either with a bar magnet or a more sophisticated magnetic device. Light- and temperature-induced actuations of the LCE particles in dependence of their MNP contents were investigated and combined with magnetic movements. It was shown that MNPs lead to a disturbance of the director alignment of the used LCE precursors and thus, LCE actuations decrease with increasing amounts of Fe_3O_4. Here, a compromise needs to be found between actuation properties (degree of actuation) and magnetic addressability (speed of guiding) in dependence of the desired application. The guidance of LCEs in magnetic fields, and the use of their different stickiness to other materials in the LC and isotropic phase allowed their usage as transport systems. Our studies show that it is possible to synthesize a huge amount of such LCE transport systems and show their potential to use them as microrobots to transport micro-objects. Admittedly, their usage to complete tasks in the human body is still a dream but it demonstrates a possible next step to reach this goal.

REFERENCES

[1] *A. Buguin, M.-H. Li, P. Silberzan, B. Ladoux, P. Keller, Micro-Actuators: When Artificial Muscles Made of Nematic Liquid Crystal Elastomers Meet Soft Lithography, J. Am. Chem. Soc. 128 (2006) 1088–1089. https://doi.org/10.1021/ja0575070.*

[2] *C. Ohm, C. Serra, R. Zentel, A Continuous Flow Synthesis of Micrometer-Sized Actuators from Liquid Crystalline Elastomers, Adv. Mater. 21 (2009) 4859–4862. https://doi.org/10.1002/adma.200901522.*

[3] *H. Yang, G. Ye, X. Wang, P. Keller, Micron-sized liquid crystalline elastomer actuators, Soft Matter. 7 (2011) 815–823. https://doi.org/10.1039/C0SM00734J.*

[4] *D.L. Polla, A.G. Erdman, W.P. Robbins, D.T. Markus, J. Diaz-Diaz, R. Rizq, Y. Nam, H.T. Brickner, A. Wang, P. Krulevitch, Microdevices in Medicine, Annu. Rev. Biomed. Eng. 2 (2000) 551–576. https://doi.org/10.1146/annurev.bioeng.2.1.551.*

[5] *C. Hu, S. Pané, B.J. Nelson, Soft Micro- and Nanorobotics, Annu. Rev. Control. Robot. Auton. Syst. 1 (2018) 53–75. https://doi.org/10.1146/annurev-control-060117-104947.*

[6] *F. Cheng, R. Yin, Y. Zhang, C.-C. Yen, Y. Yu, Fully plastic microrobots which manipulate objects using only visible light, Soft Matter. 6 (2010) 3447. https://doi.org/10.1039/c0sm00012d.*

[7] *C. Ohm, M. Brehmer, R. Zentel, Liquid Crystalline Elastomers as Actuators and Sensors, Adv. Mater. 22 (2010) 3366–3387. https://doi.org/10.1002/adma.200904059.*

[8] *A. Kaiser, M. Winkler, S. Krause, H. Finkelmann, A.M. Schmidt, Magnetoactive liquid crystal elastomer nanocomposites, J. Mater. Chem. 19 (2009) 538–543. https://doi.org/10.1039/B813120C.*

[9] *M. Warner, E.M. Terentjev, Liquid crystal elastomers, Oxford university press, 2007.*

[10] *H. Wermter, H. Finkelmann, Liquid crystalline elastomers as artificial muscles, E-Polymers. 1 (2001). https://doi.org/10.1515/epoly.2001.1.1.111.*

[11] *A.M. Schmidt, Electromagnetic Activation of Shape Memory Polymer Networks Containing Magnetic Nanoparticles, Macromol. Rapid Commun. 27 (2006) 1168–1172. https://doi.org/10.1002/marc.200600225.*

[12] *M. Winkler, A. Kaiser, S. Krause, H. Finkelmann, A.M. Schmidt, Liquid Crystal Elastomers with Magnetic Actuation, Macromol. Symp. 291–292 (2010) 186–192. https://doi.org/10.1002/masy.201050522.*

[13] *B. Klöckner, P. Daniel, M. Brehmer, W. Tremel, R. Zentel, Liquid crystalline phases from polymer functionalized ferri-magnetic Fe 3 O 4 nanorods, J. Mater. Chem. C. 5 (2017) 6688–6696. https://doi.org/10.1039/C7TC01106G.*

[14] *L.B. Braun, T. Hessberger, R. Zentel, Microfluidic synthesis of micrometer-sized photoresponsive actuators based on liquid crystalline elastomers, J. Mater. Chem. C. 4 (2016) 8670–8678. https://doi.org/10.1039/C6TC02587K.*

[15] *M.-H. Li, P. Keller, Artificial muscles based on liquid crystal elastomers, Philos. Trans. R. Soc. A Math. Phys. Eng. Sci. 364 (2006) 2763–2777. https://doi.org/10.1098/rsta.2006.1853.*

[16] *D.L. Thomsen, P. Keller, J. Naciri, R. Pink, H. Jeon, D. Shenoy, B.R. Ratna, Liquid Crystal Elastomers with Mechanical Properties of a Muscle, Macromolecules. 34 (2001) 5868–5875. https://doi.org/10.1021/ma001639q.*

[17] *O. Baun, P. Blümler, Permanent magnet system to guide superparamagnetic particles, J. Magn. Magn. Mater. 439 (2017) 294–304. https://doi.org/10.1016/j.jmmm.2017.05.001.*

02 Extraordinary Field Enhancement of TiO_2 Porous Layer up to 500-Fold

K. Yoshihara, M. Sakamoto, H. Tamamitsu, *et al.*

ABSTRACT

Titanium dioxide (TiO_2) is known as a very important material for photocatalysts, the photoelectrode for hydrogen evolution reaction, and the porous layer of perovskite solar cells. Here, extraordinary field enhancement of a porous TiO_2 layer, mesoscopic film is shown. The field enhancement is investigated with respect to the fluorescence intensity of a dye molecule and an enhancement factor (EF) of up to 500 is achieved, which corresponds to the largest EF for a semiconductor. Furthermore, EF is up to 30000 after numerical corrections. The large EF is realized for a porous TiO_2 layer composed of a specific particle size of 550 nm, which is consistent with the results of fluorescence intensity, scattering intensity, and two different theoretical calculations based on Mie scattering theory, with respect to particle size.

INTRODUCTION

When a noble metal with nanostructure is irradiated with light, localized surface plasmons are resonantly generated, which enhance various physical and chemical processes near the surface, like Raman scattering or fluorescence intensities of molecules,[1,2] also known as surface-enhanced fluorescence (SEF). The enhancement factor (EF) of SEF is much lower than that of surface-enhanced Raman scattering (SERS) due to fluorescence quenching via energy transfer from an excited dye molecule to the noble metal substrate with a high density of states. To solve this problem, cost-effective dielectric materials with opposite characteristics to noble metals are potential candidates as enhancement materials. For example, an electronically forbidden transition material, i.e., indirect transition in the bandgap of a semiconductor, can suppress energy transfer from an excited molecule to a substrate material that has the nature of an indirect-transition semiconductor as a forbidden transition.

In the present study, titanium dioxide (TiO_2) was investigated as a SEF material. TiO_2 has been an important material for photocata-

lysts,[3] the porous layer used as the scaffold to obtain good perovskite crystal as well as charge transport of perovskite solar cells,[4,5] and as the photoelectrode for the hydrogen evolution reaction[6]. As for the field enhancement of TiO_2, two studies were reported on finite-difference time-domain calculations, i.e., spherical particle[7] and nanodisk,[8] but there has been no report on porous TiO_2 layers yet so far.

Here, we demonstrate the field enhancement of a porous TiO_2 layer by measuring the SEF of dye molecules. The porous TiO_2 layer preparation consists of mechanochemical ball milling and drop casting of a TiO_2 solution.

MATERIALS AND METHODS

Preparation of TiO_2 Solution and Enhanced Substrate Using Drop Casting

TiO_2 particles were processed by a mechanical wet-process ball-milling method using a commercial planetary ball-milling apparatus (Premium line P-7, Fritsch Co., Ltd.). TiO_2 anatase powder (1 g), zirconia (ZrO2) milling balls (1 mm diameter, 40 g), and methanol (6 g) were placed in a ZrO2 milling vessel (45 mL) and ball-milled at 600 rpm for 3 h. The size of the TiO_2 particles in the solution was measured by dynamic light scattering. Solutions of the TiO_2 particles after milling were prepared by diluting with either water or methanol. The enhanced substrate was prepared by drop casting the diluted TiO_2 solution onto an indium tin oxide (ITO) glass substrate, which was cleaned with a sonicator and dried in advance. The ITO glass was used for observation of the TiO_2 layer with a scanning electron microscope (SEM). Then, the TiO_2 layer covered the ITO layer to an area that was 50 times greater than that of the focal point of light used for fluorescence measurements.

Measurements of Enhancement Spectra and Estimation of Enhancement Factor

The fluorescence spectrum of the CV dye molecule was measured with a confocal microscope spectrometer (HR800, Horiba Jobin Yvon) at an excitation wavelength of 632.8 nm using a He–Ne laser. An objective lens (SMLPLN, 100×, Olympus®) with a superlong working distance (7.6 mm) was used to measure the fluorescence spectra of the sample solution under a cover glass. The optical cell for measurement of the fluorescence spectrum was designed to give a solution layer between the cover glass and the TiO_2 layer, and was described elsewhere (see original work for references[9]). The dye solution used was CV dissolved in methanol to a concentration of 3.6×10^{-5} m. A fluorescence spectrum was obtained as the average of the number of fluorescence spectra of 10 different positions of TiO_2: a spectrum at a position was measured with 10 accumulations of the data collection time of spectrum as 1 s. The EF of fluorescence intensity was obtained by measuring four spectra: 1) the fluorescence spectrum of the CV solution with the TiO_2 layer (I1), 2) the fluorescence spectrum of the CV solution without the TiO_2 layer (I2), 3) the background spectrum of 1 with methanol as the solvent and with the TiO_2 layer (I3), and 4) the background spectrum of 2 with methanol as the solvent and without the TiO_2 layer (I4). The EF of fluorescence intensity was then obtained using these four spectra, according to EF = (I1 – I3)/(I2 – I4). EF values were obtained from the averages of 10 spectra for the I1 and the I2 and 5 spectra for the I3 and the I4, and all error bars denote to 2σ, where σ is a standard deviation from EF average. The EF was also evaluated by taking account of the penetration depth of laser light into TiO_2 layer under the condition of the same volumes probed by the laser and at the same number of CV molecules.

Evaluation and Calculation of the TiO_2 Layer

The scattering spectrum of the TiO_2 layer was measured in the darkfield using the same fluorescence microscope spectrometer. A ring-shaped halogen lamp (KL1500LCD, Carl Zeiss) equipped with an objective lens was used as the light source for the scattering measurement under darkfield conditions. To compensate for the operation of the instrumentation on the scattering spectrum, the scattering spectrum of a commercial diffuse reflector was measured as a standard spectrum. The absorption spectrum of TiO_2 layer was measured by a JASCO V-660 spectrophotometer. The obtained absorption coefficient, α, was used to calculate the penetration depth, $1/\alpha$, of the laser light into TiO_2 layer. The surface of the TiO_2 layer was analyzed by measuring height images with a laser microscope (LEXT™ OLS4000 microscope, Olympus). The height data were then used for the FDTD calculation. The electric field distribution on the surface of the TiO_2 layer was calculated using the DTD method with the FullWAVE commercial software (Cybernet Systems Co., Ltd.). The scattering efficiency Qsca, was calculated using the Mieplot software (version 4.05.02, Philip Laven). For these calculations, the refractive index of TiO_2 (anatase) at an excitation wavelength of 632.8 nm was used; n = 2.33 as the

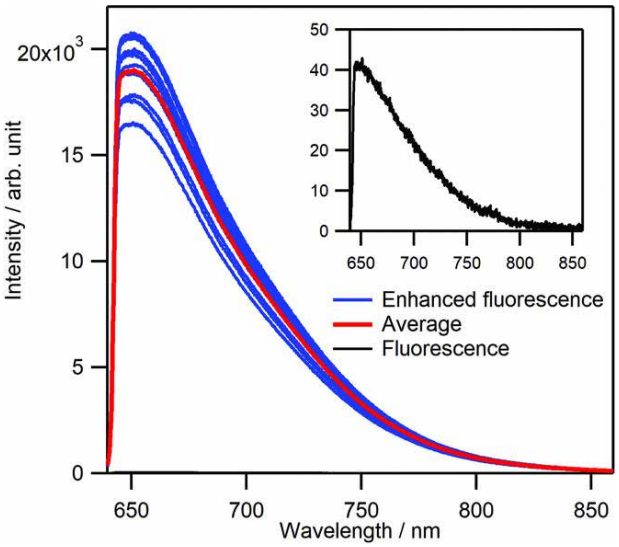

Figure 1: Fluorescence spectra of CV solution measured with (blue and red) and without (black) the TiO_2 layer. The red spectrum shows the average of the blue spectra.

real part and $\kappa = 1.6 \times 10^{-3}$ as the imaginary part, of which the values were obtained from an average of reported values. The refractive indices for gold (Au), silver (Ag), and silicon (Si) at an excitation wavelength of 632.8 nm were used as values in the software. The extinction efficiency Qext, Qext = Qabs + Qsca, was also calculated for TiO_2, Au, Ag, and Si.

See the original work and its supporting information for more experimental details[9].

RESULTS AND DISCUSSIONS

Figure 1 shows the fluorescence spectra of a crystal violet (CV) solution with (blue curve) and without (black curve) the TiO_2 layer. These data were obtained using a TiO_2 layer prepared from a solution composed of a volume ratio of water/methanol = 27. The fluorescence intensity of CV was significantly increased in the presence of the TiO_2 layer. The average and maximum EF values were estimated to be 480 and 526, respectively. Compared with EFs published for various materials and semiconductors, the EF for TiO_2 is significantly large.

Next, the TiO_2 layer was analyzed by measuring surface height images with a laser microscope. **Figure 2a, b** shows typical height images for TiO_2 layers prepared by drop casting aqueous-methanol and methanol solutions, respectively. These images reveal that the former layer has a higher surface roughness. The surface roughness was quantified by estimation of the mean height, S_a. As a result, S_a for the layer prepared from aqueous-methanol solution was 2.9 times greater than that prepared from methanol solution. In addition, S_a was also changed by the concentration of TiO_2 in a solution. Therefore, S_a can be controlled according to either the solvent or the concentration.

EFs were investigated as a function of S_a, as shown in **Figure 3a.** The results indicate that the EF increases with the surface roughness, whereas it decreases over the peak position of Sa. The maximum EF of 480 was located around S_a=0.55 µm; therefore, there is a specific size to obtain a significantly large EF (S_a

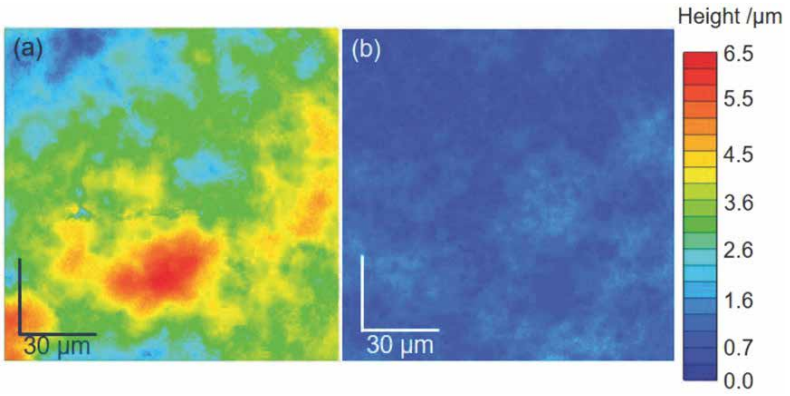

Figure 2: Laser microscope images of the surface of TiO_2 layers prepared by drop casting of TiO_2 particles from a) aqueous-methanol solution and b) methanol solution. A pixel resolution of the laser microscope is set as 126 nm × 126 nm at the x–y region.

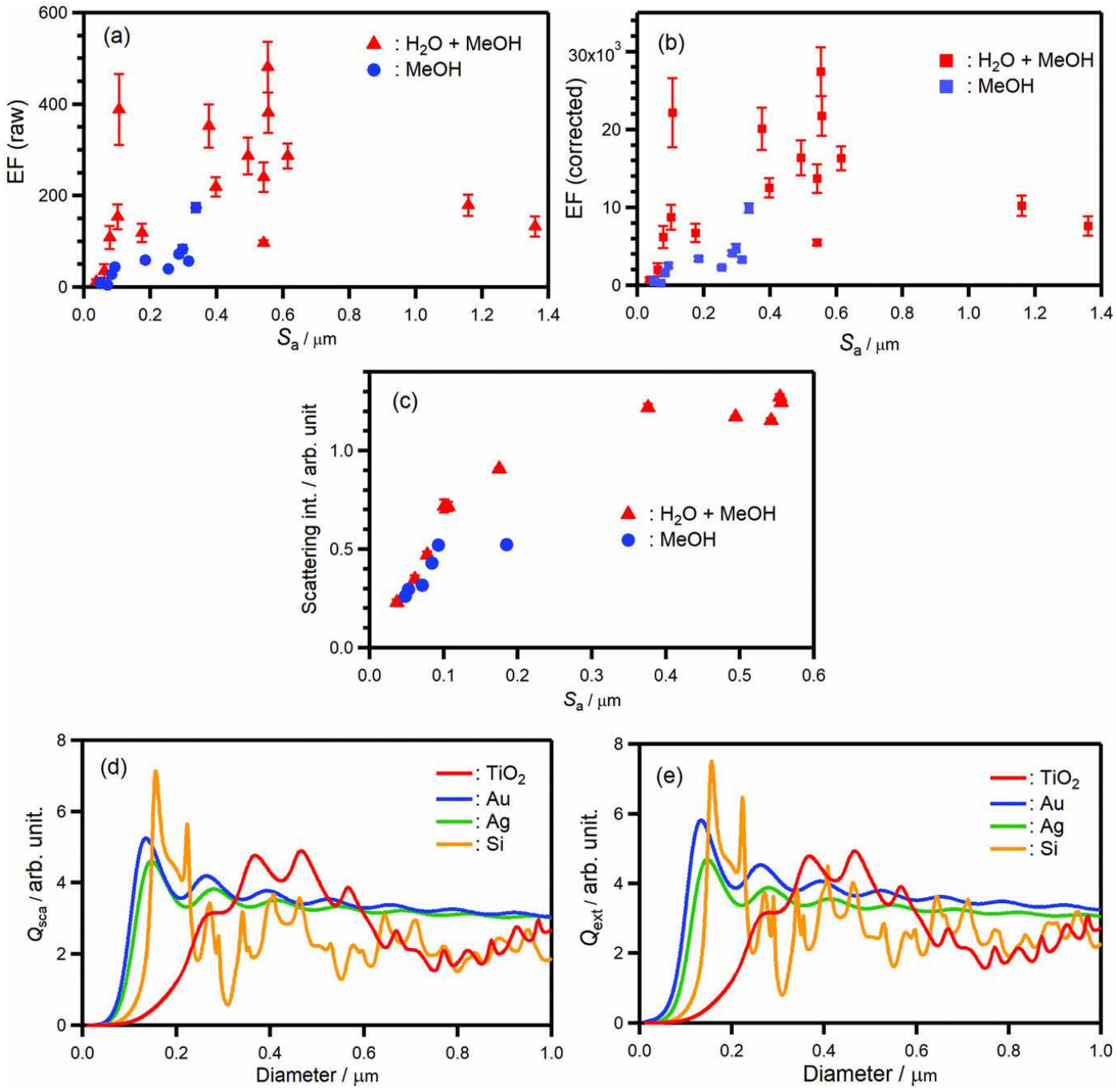

Figure 3: a) EF of TiO_2 layers prepared from drop casting aqueous-methanol and methanol solutions as a function of surface roughness. The EF values are obtained as raw data without corrections for the volumes probed by the laser and the number of CV molecules. b) EF of TiO_2 layers prepared from drop-casting aqueous-methanol and methanol solutions as a function of surface roughness. This EF indicates "EF per a CV molecule." Namely, the EF values are obtained as corrected ones using the data (a) and the solution volumes probed by laser and the number of CV molecules, i.e., the same volumes of bulk solution and solution in TiO_2 porous layer as well as the same number of molecules there. c) Scattering intensity as a function of surface roughness for TiO_2 layers prepared from drop-casting aqueous-methanol and methanol solutions. d) Qsca for particles of four materials immersed in methanol are calculated as a function of particle size (diameter). e) Q_{ext}, $Q_{ext} = Q_{sca} + Q_{abs}$, for particles of four materials immersed in methanol are calculated as a function of particle size (diameter).

is averaged height of TiO_2 particle in the z-direction. Since the TiO_2 layer is isotropic structure, the value of Sa corresponds to the size in x–y-direction and results in the size of particle). The EFs in **Figure 3a** are carefully obtained by measuring various background signals, while the EFs are treated as raw data without the corrections of solution volumes probed by the laser and the number of CV molecules. In order to analyze the EFs furthermore, we evaluated solution volumes in a bulk solution and in voids of a porous TiO_2 layer probed by the laser, both of which are estimated as 54 and 0.92 μm^3, respectively. According to the volume ratio 54/0.92 μm^3, there is 57 times difference in between the volumes as well as the number of CV molecules. **Figure 3b** shows corrected EFs under the same solution volume and the same number of CV molecules. Note that the maximum EF is up to 30,000 at around the particle size with 550 nm. Namely, this EF indicates "EF per a CV molecule."

Figure 3d shows the calculated results for the scattering efficiency Q_{sca} of a TiO_2 spherical particle dispersed in methanol as a function of the particle diameter. To compare the results for TiO_2 with those for other materials, Q_{sca} was also calculated for Ag and Au particles under the same condition. Note that Q_{sca} for TiO_2 is larger than those for Au, Ag, and Si in a specific size, and is the largest for the particle size range of 0.35–0.6 μm. Furthermore, we examined extinction efficiency Q_{ext}, $Q_{ext} = Q_{sca} + Q_{abs}$, for these materials. As a result, the value of TiO_2 is the highest at around 500 nm, as shown in **Figure 3e.** Thus, the present TiO_2 particles have a significantly high EF, which to the best of our knowledge is the largest obtained in studies on SEF using semiconductors. Moreover, we investigated field enhancements by changing particle sizes of TiO_2, Si, Au, and Ag using FDTD calculations. Namely, the EFs of these four materials were calculated on a single spherical particle, immersed in methanol, with diameters of 300, 400, 500, and 600 nm. The TiO_2 particle gives the highest EF in four materials at the diameter of 500–600 nm, whereas smaller particles of 300 nm show that Ag and Au particles give higher EFs than that of TiO_2.

To evaluate the relation between the EF and the surface structure, the electric field of the TiO_2 layer was calculated using the FDTD method. It was found that the EF is large at the surface of TiO_2 with a surface roughness of several hundred nanometers. This trend is in good agreement with the experimental data, i.e., the EF became a maximum at a surface roughness of 550 nm, as shown in **Figures 5a,** b. Therefore, according to both experimental and theoretical evidence, TiO_2 with a size of ≈500 nm results in extraordinary EF.

CONCLUSION

In summary, ball-milled TiO_2 particles were mechanically prepared and were dispersed in a solution and drop-cast to produce a TiO_2 porous layer on a glass substrate. The TiO_2 porous layer composed of particles with sizes in the range of 0.3–0.6 μm resulted in significant field enhancement, which was in good agreement with the scattering spectra and calculations using the FDTD method and Mie theory. Such a large field enhancement as EF = 500 is ascribed to the properties of TiO_2 particles with specific size (0.3–0.6 μm), such as a high refractive index, indirect transitions, hot spot, and many edges. In addition, the EF corrected, under the same solution volume probed by the laser and the same number of CV molecules, was up to 30000 at around the particle size with 550 nm. Special advantages of the present system for accomplishing such extraordinary EF are principally the following three, i) porous TiO_2 layer gives many hot spots among particles, ii) a component of porous layer is particles with the size of around 500 nm that can give the maximum field enhancement, iii) particles with many edges giving higher electric field.

REFERENCES

[1] *S.A. Maier, Plasmonics: fundamentals and applications, Springer Science \& Business Media, 2007.*

[2] *K. Aslan, C.D. Geddes, Metal-enhanced fluorescence: progress towards a unified plasmon-fluorophore description, John Wiley \& Sons, Inc: Hoboken, NJ, 2010.*

[3] *U.I. Gaya, A.H. Abdullah, Heterogeneous photocatalytic degradation of organic contaminants over titanium dioxide: A review of fundamentals, progress and problems, J. Photochem. Photobiol. C Photochem. Rev. 9 (2008) 1–12. https://doi.org/10.1016/j.jphotochemrev.2007.12.003.*

[4] *G. Kakavelakis, K. Petridis, E. Kymakis, Recent advances in plasmonic metal and rare-earth-element upconversion nanoparticle doped perovskite solar cells, J. Mater. Chem. A. 5 (2017) 21604–21624. https://doi.org/10.1039/C7TA05428A.*

[5] *T. Miyasaka, Toward Printable Sensitized Mesoscopic Solar Cells: Light-Harvesting Management with Thin TiO 2 Films, J. Phys. Chem. Lett. 2 (2011) 262–269. https://doi.org/10.1021/jz101424p.*

[6] *R. Abe, Recent progress on photocatalytic and photoelectrochemical water splitting under visible light irradiation, J. Photochem. Photobiol. C Photochem. Rev. 11 (2010) 179–209. https://doi.org/10.1016/j.jphotochemrev.2011.02.003.*

[7] *Y. Tanaka, G. Obara, A. Zenidaka, N.N. Nedyalkov, M. Terakawa, M. Obara, Near-field interaction of two-dimensional high-permittivity spherical particle arrays on substrate in the Mie resonance scattering domain, Opt. Express. 18 (2010) 27226. https://doi.org/10.1364/OE.18.027226.*

[8] *H.-J. Lin, K. de Oliveira Lima, P. Gredin, M. Mortier, L. Billot, Z. Chen, L. Aigouy, Fluorescence enhancement near single TiO 2 nanodisks, Appl. Phys. Lett. 111 (2017) 251109. https://doi.org/10.1063/1.4994311.*

[9] *K. Yoshihara, M. Sakamoto, H. Tamamitsu, M. Arakawa, K. Saitow, Extraordinary Field Enhancement of TiO 2 Porous Layer up to 500–Fold, Adv. Opt. Mater. 6 (2018) 1800462. https://doi.org/10.1002/adom.201800462.*

03 $NaMgF_3:Tb^{3+}@NaMgF_3$ Nanoparticles Containing Deep Traps for Optical Information Storage

Y. Wang, D. Chen, Y. Zhuang, *et al.*

ABSTRACT

Persistent luminescence materials containing deep traps have attracted attention in the field of optical information storage. However, the lack of nanomaterials with satisfactory light storage ability has become one of the main obstacles to practical applications. In this work, $NaMgF_3:Tb^{3+}@NaMgF_3:Tb^{3+}$ nanoparticles are reported that exhibit excellent light storage ability into deep traps upon X-ray irradiation and controllable photon emissions under thermal stimulation. A surface passivation strategy by constructing a core–shell structure is adopted, which is proved valid to greatly enhance the PersL efficiency. Due to the excellent dispersibility and stability in water, luminescent inks containing the nanoparticles are successfully prepared and the applications to inkjet printing optical information storage and information decryption are demonstrated.

INTRODUCTION

Magnetic storage, semiconductor memory, and optical information storage are the three main storage technologies in the information age.[1,2] Among them, optical information storage shows the advantages of low production cost, low energy consumption, excellent resistance to external interference, and long storage life; thus it is widely used in the long-term storage of large amounts of data that are not modified frequently.[3,4] However, due to the diffraction limit, the storage capacity of the traditional 2D optical information storage technology (such as Blu-ray discs) has been difficult to make a big breakthrough.[5]

Persistent luminescence (PersL) materials are a kind of phosphor with light storage ability and delayed photon emissions under thermal or photostimulation.[6-8] When the trap depths of the PersL materials are sufficiently deep, the charge carriers could be frozen in the traps at room temperature (RT) for a long duration, thus enabling long-term optical information storage. In the past few years,

a lot of work has been done on developing new materials and exploring their applications in multifunctional optical information storage.[9,10] Designing new PersL materials with nanoscale and deep traps is of great significance for the development of high-capacity optical information storage technology. At present, there are few reports on the nanoparticles with excellent PersL performance. One of the main reasons could be serious PersL quenching and structural instability when the particle size is decreased to nanoscale.

It has been reported that $NaMgF_3$ is a kind of material with good X-ray absorption ability.[11,12] Besides, the emission spectra of the NaMgF3 matrix could be tailored with considerable flexibility, and the application scenarios of this material are accordingly further expanded. However, the energy storage capacity of lanthanide-doped $NaMgF_3$ nanoparticles under X-ray irradiation has not been thoroughly reported, although many important applications such as photobiomedical detection and high-throughput optical information storage may emerge. In this work, we reported fluoride nanoparticles $NaMgF_3:Tb^{3+}$ containing deep traps for light storage and demonstrated their applications to optical information storage by using an inkjet printing technology.

MATERIALS AND METHODS

Raw Materials and Chemicals

$Mg(NO_3)_2{\cdot}6H_2O$ (99.9%), $Tb(NO_3)3{\cdot}5H_2O$ (99.9%,), and oleic acid (OA, A.R.) were purchased from Aladdin Corporation. NaF (99.99%) was purchased from Macklin Corporation. All the materials were directly used without further purification. Synthesis of $NaMgF_3:Tb^{3+}$ Nanoparticles: $NaMg^{1-x}F_3:xTb^{3+}$ (x = 0.06–0.3, with a concentration gradient of 0.03) nanoparticles were synthesized by using a hydrothermal reported in the literature with some modifications (see original work and its supporting information for references) 1, 1.5, and 2 times of the original reactant concentrations were compared, and 1.5 times was chosen as the optimal condition as the composition plan in this work. Briefly, stoichiometric $Mg(NO_3)_2{\cdot}6H_2O$ and $Tb(NO_3)_3{\cdot}5H_2O$ (the total amount of Mg and Tb cations was 5 mmol) were dissolved into 5 mL deionized water. 4.5 mL oleic acid was added dropwise into the cationic solution and kept stirring for 10 min to produce oleic-acid-based complex compounds. Another anion solution containing 15 mmol NaF and 5 mL deionized water was added dropwise into the above solution, stirred at 600 rpm for 1 h to form a milky colloidal solution. The solution was transferred to a 40 mL Teflon-lined autoclave, sealed, and kept at 160 °C (320 °F) for 12 h. After cooling to RT, white products were collected by centrifugation. To remove remaining organic ligands, first, the products were washed with deionized water/ethanol for three times and dispersed with 6 mL acetone, respectively. Then, add 250 µL hydrochloric acid (0.1 mol L–1) into each solution followed with an ultrasonic oscillation for 2 h at RT. Lastly, the products were washed again with deionized water/ethanol three times. The final products of $NaMgF_3:Tb^{3+}$ nanoparticles (≈521 mg) were dispersed into 12 mL ethanol for further use.

Synthesis of $NaMgF_3:Tb^{3+}@NaMgF_3$ Core–Shell Nanoparticles

The synthesized $NaMgF_3:Tb^3$ nanoparticles in ethanol (12 mL) was mixed with 0.5 mmol $Mg(NO_3)_2{\cdot}6H_2O$, 1.5 mmol NaF, and 4.5 mL OA. The mixture was transferred into a 40 mL Teflon-lined autoclave and stirred for 10 min. The autoclave was sealed and kept at 160 °C (320 °F) for 12 h. After cooling to RT, white products were collected by centrifugation. The products were washed with deionized water/ethanol for three times, treated with hydrochloric acid (0.1 mol L–1) to remove remaining organic ligands, and washed again with deionized water/ethanol for three times. The final products of $NaMgF_3:Tb^{3+}@NaMgF_3$ core–shell nanoparticles were obtained by drying in an oven at 60 °C (140 °F) overnight.

Preparation of Luminescent Inks Containing Nanoparticles and Setup for Inkjet Printing

The synthesized $NaMgF_3:Tb^{3+}@NaMgF_3$ nanoparticles (100 mg) were dispersed into 5 mL deionized water and stirred thoroughly to prepare a luminescent ink. The aqueous ink could be kept at RT for 14 d without obvious precipitation. The ink was then loaded into an inkjet printing system (MicroFab, Jetlab@4). A 50 µm diameter piezoelectric-type nozzle was selected. The driving voltage waveforms and negative pressure values of the inkjet printer were adjusted to generate stable and continuous droplets. The spatial accuracy of the inkjet printing system was ≈5 µm. A sapphire single crystal sheet (ϕ30 mm × 1 mm) was placed under the printing nozzle. The temperature of the substrate was set to 40 °C (104 °F). Typically, a customer-designed pattern was inkjet-printed on the sapphire substrate. The printed pat-

tern was irradiated by an X-ray source (average dose rate ≈2.58 μSv s−1) or 5 min and kept in the dark at RT for further use. Finally, a PersL image was reproduced by heating to 400 K and recorded with a digital camera.

Structural and Optical Characterizations

Powder XRD patterns of the nanoparticles were recorded by using an X-ray diffractometer (Bruker, D8 Advance) with Cu Kα radiation at an interval of 0.02° with a scanning speed of 10° min^{-1}. The particle morphology and microstructure were observed using a field-emission transmission electron microscope (Talos F200s). PL and PLE spectra were measured with a spectrophotometer (Edinburgh Instrument, FLS980); all samples were tested in dry powders. The RL spectra were recorded with a fiber spectrophotometer (Ocean Optics, QE Pro). The PersL decay curves and PersL spectra were recorded with a home-built measurement system driven by a LabVIEW-based program. In this system, a portable X-ray tube (Amptek, Mini-X2) with a maximum output of 10 W (typical voltage 50 kV, tube current 0.2 mA, and average dose rate ≈2.58 μSv s−1) was used as the excitation source to generate PersL. A filter-attached photomultiplier tube (PMT, Hamamatsu, R928P) and a fiber spectrophotometer (Ocean Optics, QE Pro) were applied to record the PersL intensity and spectra, respectively. The TL glow curves were recorded using another LabVIEW program driven measurement system. Briefly, the sample was irradiated by the X-ray source for 5 min (total dose ≈774 μSv) at 250 K. After removing the excitation source, the TL signals were recorded by the PMT detector from 250 to 550 K. The temperature of the sample was controlled by using a cooling/heating stage (Linkam, THMS600E). The TL spectra at different temperature were monitored by the above fiber spectrophotometer. Fluorescence microscopic images were taken by a fluorescent microscope (Olympus®, BX53M microscope). Photographic images of the samples under daylight or the PersL images were taken with a digital camera (Canon, EOS 5D Mark II) in all-manual modes.

RESULTS AND DISCUSSION

Phase Analysis and Optical Characterization of $NaMgF_3:Tb^{3+}$ Nanoparticles

The X-ray diffraction patterns of the $NaMgF_3:Tb^{3+}$ nanoparticles with 24% Tb^{3+} concentration were in good agreement with the standard diffraction patterns of $NaMgF_3$. A slight diffraction shift observed suggest unit cell expansion due to the substitution of larger Tb^{3+} ions. The $NaMgF_3$ crystal belongs to an orthorhombic perovskite structure with a space group of *Pbnm*.[13] The crystal is composed of corner-connected MgF_6 octahedrons and NaF_8 polyhedrons. Moreover, the consistency between X-ray-excited luminescence (RL) and photoluminescence (PL) spectra verified that X-ray was an efficient excitation source to give green emissions for $NaMgF_3:Tb^{3+}$. The transmission electron microscopy (TEM) images of the $NaMgF_3:Tb^{3+}$ nanoparticles showed uniform and cubic morphology with an average size of ≈18.0 nm. The energy dispersive spectroscopy analysis of elemental mapping showed the measured compositions of 21.9% (Na), 17.5% (Mg), 55.7% (F), and 4.9% (Tb).

Optimizing the Doping Concentration of Tb^{3+}

Several $NaMgF_3:Tb^{3+}$ nanoparticles with different Tb^{3+} concentrations were synthesized. With the increase of the Tb^{3+} concentration, the cell lattice expanded, resulting in a gradual shift of the XRD peaks toward the small-angle direction. Also, the PL intensity was enhanced with increasing the Tb^{3+} concentration and reached the maximum at 24%. The highest thermoluminescence (TL) intensity was found in the nanoparticles with 21% of Tb^{3+} doping. With the increasing of Tb^{3+} concentration, the average distance between the luminescent centers and emission quenchers could be reduced and energy transfer rate was increased, which resulted in the concentration quenching of PL intensity and TL intensity. The $NaMgF_3:Tb^{3+}$ nanoparticles with 24% Tb^{3+} were used in the following sections.

Constructing a Core–Shell Structure in Nanoparticles

In this section, we adopted a surface passivation strategy by constructing a core–shell structure in nanoparticles. Specifically, the synthesized $NaMgF_3:Tb^{3+}$ nanoparticles were used as the cores to grow a nonadoped $NaMgF_3$ shell (**Figure 1a**).

The TEM examinations indicated that the average size of the nanoparticles was increased from 18.0 (cores) to 19.2 (1/50), 20.0 nm (1/10), and 20.4 nm (**Figure 1b**). Accordingly, the thickness of the $NaMgF_3$ passivation shell was determined as 1.2 nm (1/50), 2.0 nm (1/10), and 2.4 nm (1/5), respectively. Also, the XRD patterns confirmed that pure phase of $NaMgF_3$ was remained in the core–shell nanoparticles (**Figure 1c**).

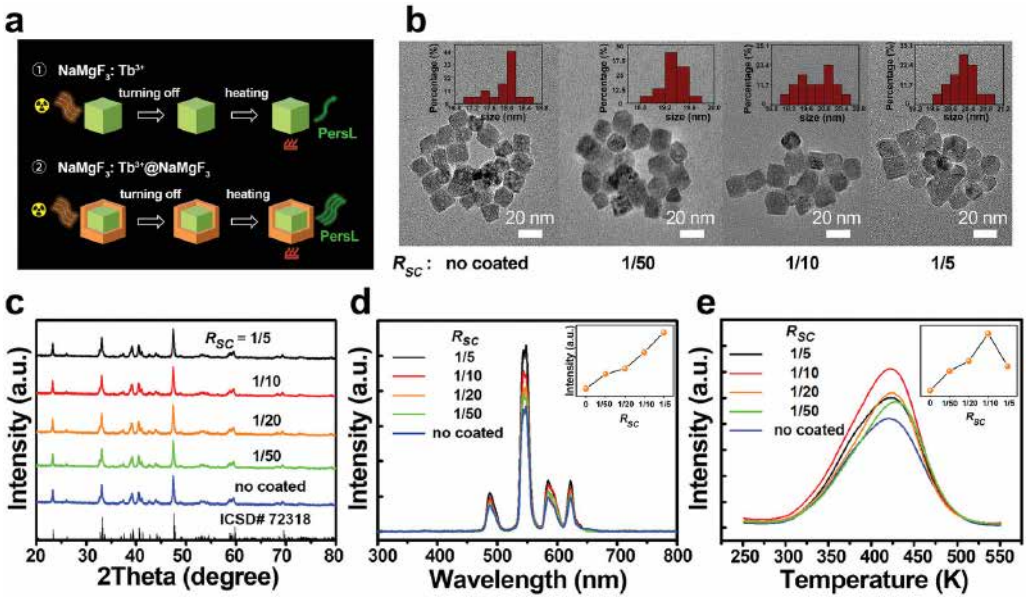

Figure 1: $NaMgF_3$:Tb^{3+}@$NaMgF_3$ nanoparticles with a core–shell structure. a) Schematic illustration of the core–shell structure and the PersL improvement. Surface quenchers on the shells were separated from the Tb^{3+} emitters inside the cores. b) TEM images of the $NaMgF_3$:Tb^{3+}@$NaMgF_3$ nanoparticles. The insets show the particle size distribution of the nanoparticles. c) XRD patterns, d) PL spectra, and e) TL glow curves of the nanoparticles with different *RSC*.

Figure 1d shows that the PL intensity of the nanoparticles under excitation of 297 nm was clearly enhanced after coating the shells. Also, the shape of the TL glow curves was independent on the shell thickness, suggesting that no new trap was introduced by the shell layer (**Figure 1e**). On the other hand, the TL intensity was also improved with increasing the shell thickness. Based on the above results, we consider that the improvement of TL should be similar to the PL enhancement due to the inhibition of energy transfer to surface quenchers.

Optical Information Storage Applications

Figure 2a shows the photographic images of the luminescent ink containing the $NaMgF_3$:Tb^{3+}@$NaMgF_3$ nanoparticles. The ink had been left standing for 7 d before use, and no obvious stratification was observed. Under X-ray irradiation, the ink gave bright green emission. Furthermore, the ink was loaded into an inkjet printing system. A pattern of the Xiamen University logo with a size of Ø10 mm was printed on a sapphire substrate (information writing, **Figure 2b**). Under the fluorescence microscope (under excitation at 405 nm), one could see that the printed pattern was composed of small dots in an orthogonal array. The dots showed a regular circular morphology and a diameter of ≈100 μm (**Figure 2c**).

The sapphire substrate was placed under X-ray irradiation for energy charging (5 min). As shown in **Figure 2d,** a luminescent pattern was clearly observed under X-ray irradiation, and it quickly faded once the excitation source was turned off. The X-ray-charged pattern was kept in the dark at RT for 10 min and moved to a heater preset at 400 K. After taking several seconds for heat conduction, the stored pattern on the sapphire substrate was reproduced and recorded by a digital camera (information readout, **Figure 2d**).

Furthermore, the delayed emission of the PersL nanoparticles could be used in information encryption and decryption. As schematically illustrated in **Figure 2e,** a specific pattern made of inkjet-printed $NaMgF_3$:Tb^{3+}@$NaMgF_3$ nanoparticles was written on the substrate. The pattern was then covered with a full layer of CdSe quantum dots. Since the CdSe and $NaMgF_3$:Tb^{3+}@$NaMgF_3$ both gave green emission under UV and X-ray irradiation, the pattern was well hidden (being an unreadable state, **Figure 2f**). On the other hand, only the $NaMgF_3$:Tb^{3+}@$NaMgF_3$ nanopar-

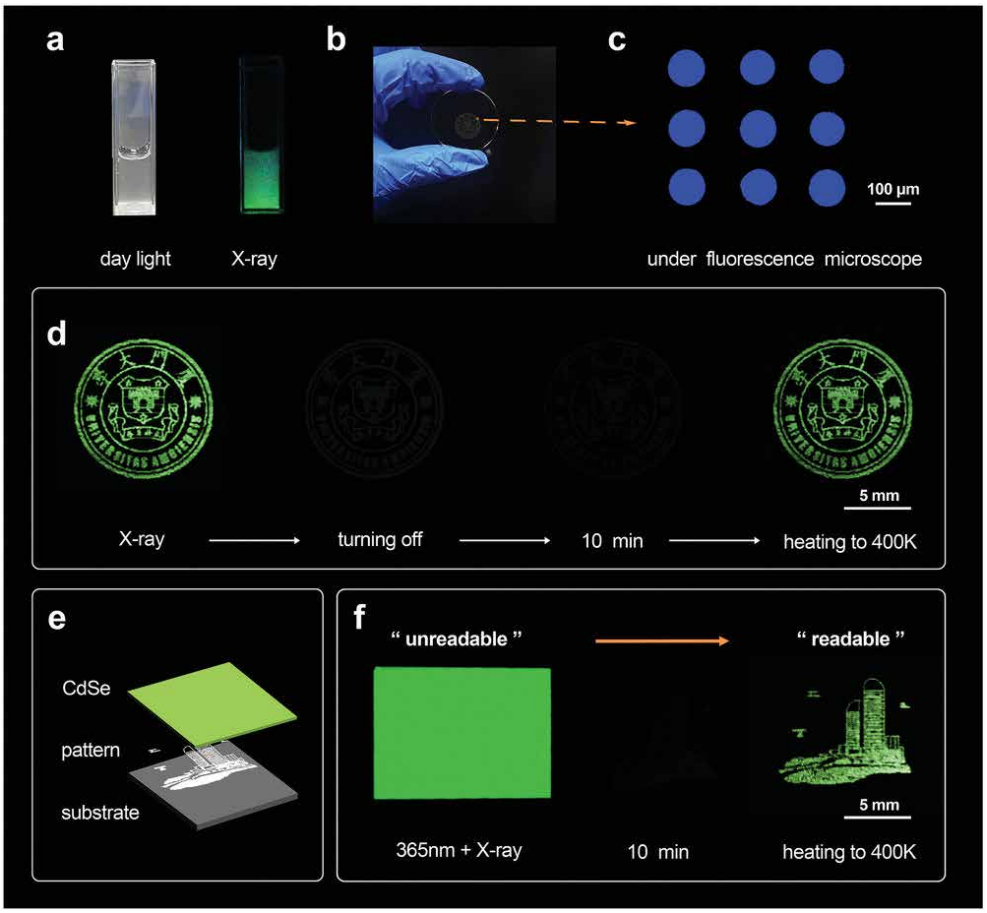

Figure 2: Applications of the $NaMgF_3:Tb^{3+}@NaMgF_3$ nanoparticles to optical information storage and information encryption. a) Photographs of the luminescent ink under day light and X-ray irradiation. The ink was left standing for 7 d before use. b) Photograph of a sapphire substrate after printing with a Xiamen University logo. c) Image of the printed pixels under fluorescence microscope. d) Photographs of the emission images during X-ray irradiation, at the moment of turning off, with a delay time of 10 min, and heated to 400 K. e) Schematic illustration of the optical information encryption and decryption. f) Photographs of the emission images during UV (365 nm) + X-ray irradiation, turning off with a delay time of 10 min, and heated to 400 K. The encrypted information was unreadable during irradiation and turned into readable after heating. Exposure time for (d: X-ray), (d: heating), (f: 365 nm + X-ray), (f: heating) was 3 s, respectively.

ticles were able to store irradiation energy. When the substrate was heated to 400 K consequently, the $NaMgF_3:Tb^{3+}@NaMgF_3$ gave PersL and decrypt the recorded information (tuning to a readable state, **Figure 2f**).

CONCLUSION

In this work, we reported a new type of PersL nanoparticles $NaMgF_3:Tb^{3+}$, which exhibited nanocubic morphology, excellent aqueous dispersibility, and light storage ability in deep traps under X-ray irradiation. These outstanding features enabled the developed nanoparticles to be applied to inkjet printing technology. Due to the light storage ability and delayed photon emissions, the $NaMgF_3:Tb^{3+}@NaMgF_3$ nanoparticles exhibited a broad prospect in the optical information storage and information encryption applications. The developed $NaMgF_3:Tb^{3+}@NaMgF_3$ nanoparticles with nanoscale size and deep traps for energy storage may open up new opportunities for advanced optical materials for the applications of information technology.

REFERENCES

[1] *M. Gu, Q. Zhang, S. Lamon, Nanomaterials for optical data storage, Nat. Rev. Mater. 1 (2016) 16070. https://doi.org/10.1038/natrevmats.2016.70.*

[2] *M. Gu, X. Li, Y. Cao, Optical storage arrays: a perspective for future big data storage, Light Sci. Appl. 3 (2014) e177–e177. https://doi.org/10.1038/lsa.2014.58.*

[3] *S. Kawata, Y. Kawata, Three-Dimensional Optical Data Storage Using Photochromic Materials, Chem. Rev. 100 (2000) 1777–1788. https://doi.org/10.1021/cr980073p.*

[4] *Y. Katsurada, S. Hirata, K. Totani, T. Watanabe, M. Vacha, Phosphorescence: Photoreversible On-Off Recording of Persistent Room-Temperature Phosphorescence, Adv. Opt. Mater. 3 (2015) 1802–1802. https://doi.org/10.1002/adom.201570080.*

[5] *Y. Zhou, Y. Chen, H. He, J. Liao, H.T.T. Duong, M. Parviz, D. Jin, A homogeneous DNA assay by recovering inhibited emission of rare earth ions-doped upconversion nanoparticles, J. Rare Earths. 37 (2019) 11–18. https://doi.org/10.1016/j.jre.2018.05.008.*

[6] *V. Boiko, J. Zeler, M. Markowska, Z. Dai, A. Gerus, P. Bolek, E. Zych, D. Hreniak, Persistent luminescence from Y3Al2Ga3O12 doped with Ce3+ and Cr3+ after X-ray and blue light irradiation, J. Rare Earths. 37 (2019) 1200–1205. https://doi.org/10.1016/j.jre.2019.03.010.*

[7] *J. Xu, S. Tanabe, Persistent luminescence instead of phosphorescence: History, mechanism, and perspective, J. Lumin. 205 (2019) 581–620. https://doi.org/10.1016/j.jlumin.2018.09.047.*

[8] *X. Zhang, Z. Quan, J. Yang, P. Yang, H. Lian, J. Lin, Solvothermal synthesis of well-dispersed NaMgF3 nanocrystals and their optical properties, J. Colloid Interface Sci. 329 (2009) 103–106. https://doi.org/10.1016/j.jcis.2008.09.076.*

[9] *Y. Zhuang, L. Wang, Y. Lv, T.-L. Zhou, R.-J. Xie, Optical Data Storage and Multicolor Emission Readout on Flexible Films Using Deep-Trap Persistent Luminescence Materials, Adv. Funct. Mater. 28 (2018) 1705769. https://doi.org/10.1002/adfm.201705769.*

[10] *Z. Long, Y. Wen, J. Zhou, J. Qiu, H. Wu, X. Xu, X. Yu, D. Zhou, J. Yu, Q. Wang, No-Interference Reading for Optical Information Storage and Ultra-Multiple Anti-Counterfeiting Applications by Designing Targeted Recombination in Charge Carrier Trapping Phosphors, Adv. Opt. Mater. 7 (2019) 1900006. https://doi.org/10.1002/adom.201900006.*

[11] *G.V.M. Williams, S. Janssens, C. Gaedtke, S.G. Raymond, D. Clarke, Observation of photoluminescence and radioluminescence in Eu and Mn doped NaMgF3 nanoparticles, J. Lumin. 143 (2013) 219–225. https://doi.org/10.1016/j.jlumin.2013.05.016.*

[12] *J.J. Schuyt, G.V.M. Williams, Photoluminescence of Dy3+ and Dy2+ in NaMgF3:Dy: A potential infrared radiophotoluminescence dosimeter, Radiat. Meas. 134 (2020) 106326. https://doi.org/10.1016/j.radmeas.2020.106326.*

[13] *X. Peng, M.C. Schlamp, A. V. Kadavanich, A.P. Alivisatos, Epitaxial Growth of Highly Luminescent CdSe/CdS Core/Shell Nanocrystals with Photostability and Electronic Accessibility, J. Am. Chem. Soc. 119 (1997) 7019–7029. https://doi.org/10.1021/ja970754m.*

Industrial Microscope Solutions

Industrial microscopes are a vital tool used for measuring, quality control, inspection, and in soldering and manufacturing. Each industrial microscope we offer uses complex designs that provide unique solutions for the inspection process and aim to improve resolution and sample contrast. Olympus industrial inspection microscopes are suited to a wide variety of analysis applications, from routine inspection to sophisticated analysis, using superb optics for industry-leading performance. We have digital microscopes and software for streamlined workflows and flexible image acquisition solutions.

CLEANLINESS INSPECTOR: OLYMPUS CIX100

Olympus' expertise in imaging and metrology systems provides today's manufacturers with solutions for particle counting, sizing and classification.

The OLYMPUS CIX100 inspection system is a dedicated, turnkey solution for manufacturers who maintain the high quality standards for the cleanliness of manufactured components. Quickly acquire, process, and document technical cleanliness inspection data to comply with company and international standards. The system's intuitive software guides users through each step of the process so even novice operators can acquire cleanliness data quickly and easily.

LEXT™ OLS5100 3D LASER SCANNING MICROSCOPE

Olympus laser confocal microscopes offer superb image quality and accurate 3D measurement by non destructive observation method with advanced optical system. Its operation preparation is easy and no pre-process is necessary with your samples.

Built for failure analysis and material engineering research, the OLS5100 laser microscope combines exceptional measurement accuracy and optical performance with smart tools that make the microscope easy to use. Precisely measure shape and surface roughness at the submicron level quickly and efficiently to simplify your workflow with data you can trust.